Received: 4 February 2022 | Revised: 18 February 2022 | Accepted: 1 March 2022

DOI: 10.1002/eom2.12201

RESEARCH ARTICLE

EcoMat WILEY

Atomic substitution effects of inorganic perovskites for optoelectronic properties modulations

Baian Chen[1,2] | **Mingzi Sun**[1] | **Rui Chen**[2] | **Bolong Huang**[1]

[1]Department of Applied Biology and Chemical Technology, The Hong Kong Polytechnic University, Kowloon, Hong Kong, China

[2]Department of Electrical and Electronic Engineering, Southern University of Science and Technology, Shenzhen, China

Correspondence
Bolong Huang, Department of Applied Biology and Chemical Technology, The Hong Kong Polytechnic, University, Hung Hom, Kowloon, Hong Kong SAR, China.
Email: bhuang@polyu.edu.hk

Rui Chen, Department of Electrical and Electronic Engineering, Southern University of Science and Technology, Shenzhen 518055, China.
E-mail: chenr@sustech.edu.cn

Funding information
Projects of Strategic Importance of the Hong Kong Polytechnic University, Grant/Award Number: 1-ZE2V; NSFC/RGC Joint Research Scheme Project, Grant/Award Number: N_PolyU502/21; National Key R&D Program of China, Grant/Award Number: 2021YFA1501101

Abstract

Inorganic perovskites exhibit impressive optoelectronic properties through experimental doping or composition modification. However, the underlying mechanism of the atomic substitution effect needs to be elucidated to guide future device optimizations. In this work, we have carried out systematic research on a series of inorganic perovskites regarding their electronic, optical, and vibrational properties. The band structures are strongly affected by the B-sites. Meanwhile, phonon dispersions have revealed that the peculiar energy band offset is determined by the varied orbital and bonding characteristics. In addition, optical properties are directly influenced by the bond lengths between B-sites and halogens, which are regulated by atomic substitutions. In addition, the infrared active spectrum and corresponding vibration modes indicate that the metal-halogen octahedrons were confirmed to be the main source of these vibration modes. This work reveals the atomic substation effects of inorganic perovskites, which offer significant guidance for the design of next-generation optoelectronic devices.

KEYWORDS

atomic substitution effect, density functional theory, inorganic perovskites, optoelectronic properties, phonon dispersion

1 | INTRODUCTION

The halide perovskites have obtained great attention as the candidate materials of electronic devices in recent years because of their impressive electronic and optical properties such as long carrier lifetime, large diffusion coefficient, and strong light absorption.[1–7] As reported in 2019, the power conversion efficiency (PCE) of perovskite solar cells has exceeded 23%, which is almost equal to that of silicon-based solar cells.[8] Meanwhile, the emerging halide perovskites also have wide potential applications such as field-effect transistors, optoelectronic sensors, and light-emitting diodes.[9–11] Although conventional experimental methods are still the cornerstone of perovskite research, emerging computational materials science is attracting increasing attention because of its convenience and low cost. To date, growing studies started to use the density functional theory to explore and predict the relationship between the macroscopic performance of perovskites and their physical nature.[12–14] By applying first-principles calculations, the enhanced photoluminescence quantum efficiency of zero-dimensional

halides perovskites was confirmed to be closely related to the decreasing of exciton migration.[15] Besides, the ab initio calculations can provide reasonable evidence of the electron–phonon coupling in the hybrid lead halide perovskites.[16] These theoretical works correlate well with the conventional experimental conclusions and exhibit the strong suitability of density functional theory for describing the intrinsic properties of perovskites.

Cs-based inorganic perovskites exhibit excellent optoelectronic properties with simple synthesis processes and controllable computational volume. Therefore, they gained much attention in both experimental and theoretical studies.[12,17–19] Yong and colleagues successfully fabricated the thermodynamically stabilized $CsPbI_3$-based solar cells with high efficiency (>18%) in 2019.[17] By applying surface treatment with choline iodide, they reduced the cracks and pinholes in the perovskite layer and thus improved the carrier lifetime. Yang et al. have pointed out that the octahedral tilting will induce vibrational instabilities by proposing the lattice calculations for $CsSnX_3$ and $CsPbX_3$ (X = F, Cl, Br, I) based on quantum chemical force constants.[20] The high-temperature phase transition of $CsSnCl_3$ was also reported before as well as the semimetal-semiconductor phase transition of $CsSnBr_3$.[21] Some essential physical issues of $CsSnX_3$ and $CsPbX_3$ (X = F, Cl, Br, I), such as the structural, electronic, and optical properties, were tested to find out the exact nature of their intrinsic characteristics.[22–24] By applying the effective-mass model and group theory, Michael et al. demonstrated a highly emissive triplet state of lowest exciton involved in $CsPbX_3$ (X = Cl, Br, I).[23] They further confirmed the bright triplet exciton with the detailed analysis of the corresponding low-temperature fluorescence spectra. In addition, the elastic anisotropy properties of $CsXBr_3$ (X = Ca, Ge, Sn) have also been visualized and studied by Brik.[22] These studies, which have conducted the computational methodology, highlighted the validity of Cs-based inorganic perovskites as the research objects for exploring basic physical characteristics of perovskite materials. By using first-principles calculations, Yuan et al. proved that the valence band maximum of halide perovskites ABX_3 is made up by an antibonding hybridization of B-*s* orbitals and X-*p* orbitals, whereas the conduction band minimum is dominated by the π antibonding of B and X *p* orbitals.[25] Crespo especially addressed the atomic and orbital contributions of halide anion on the optical properties of organic lead halide perovskites, which concludes that the Pb–Pb intra-species transitions contribute most to the light absorption.[26] Although these works have stated the influence of atomic composition and influences of bonding orbitals on the optoelectronic properties of halide perovskites, detailed connections between atomic composition and dielectric function, have not been pointed out. More effective evidence is still needed to support their physical mechanism decoding. Another essential factor of these promising materials is the phonon band structure, which has been paid increasing attention in recent years.[16,27–29] In fact, the phonon–electron interaction patterns, which are used to describe the vibrational features, are confirmed to affect the dielectric and photoelectric properties of semiconductors significantly.[30] Yang et al. argued that the phonon bandgap of organic perovskites will hinder the up-conversion of low-frequency phonons, which induces the hot-phonon bottleneck effect to prolong the lifetime of carriers.[31] This result revealed the potential phonon conversion dynamics and constructed the energy transferring model between phonons and electrons. Notably, the electron–phonon coupling nature was also reported in recent years to play an important role in the formation process of self-trapped excitons as well as the exciton emission, especially in some low-dimensional double perovskite materials.[32–34] These promising materials own similar lattice structure and extended array of corner-sharing metal halide octahedra compared with conventional perovskites but with different B-site metal atoms alternately. Strong electron–phonon coupling effect can induce considerable "transient" lattice defects to trap the primary excitons, which process can be enhanced by designing the phonon structure.[33] These studies provide a good perspective for the understanding of phonon–electron coupling mechanisms in semiconductors. However, the phonon distribution, as well as the vibration modes of inorganic perovskites $CsSnX_3$ and $CsPbX_3$ (X = F, Cl, Br, I), have not been thoroughly discussed yet. Although ample studies have investigated the role of A-site cations in the photoelectric properties of perovskites,[14,35] doping or substitution of the B-site metal and halogen atoms are still more commonly used as a means of modification engineering of perovskite materials.[36–39] The exact atomic contribution to the optoelectronic and vibrational properties of perovskites remains obscure. There is an actual need to systematically clarify the electronic, optical, and vibrational characteristics of perovskites to guide the further exploration of their potential physical abilities.

To bridge the research gap, we have studied the structural, electronic, optical, and vibrational properties of cubic phase perovskites $CsPbBr_3$, $CsPbI_3$, $CsSnBr_3$, and $CsSnI_3$ in this work. The detailed electronic, optical, and vibrational performance of these perovskites will be discussed in the main content. The theoretical investigation results contribute to revealing the physical nature of these intriguing materials and offer meaningful theoretical guidance.

2 | RESULTS AND DISCUSSION

Energy band structure determines many crucial electronic properties of materials, such as the bandgap value and energy transfer process.[40] In this section, the energy band diagrams of these perovskites were proposed firstly to investigate their basic electronic properties. The density of states (DOS) diagrams were also plotted to further explore the atomic contribution of their orbital structure. Moreover, we carried out the computed difference charge density and atomic population to provide more information for the subsequent analysis. The complex dielectric function contains key response information of materials to the incident light in different energy ranges, which can be used to derive some essential optical parameters such as the infraction index. To examine the optical characteristics of these perovskites, we compared their complex dielectric function as well as other optical parameters in this work and discussed the corresponding influence induced by atomic substitution. Phonon characteristics of these perovskites describe their lattice vibrational features and imply the potential carrier-phonon interaction.[30] Therefore, we further conducted the phonon dispersion calculations of these perovskites. Sn-based perovskites exhibit fewer imaginary frequency phonons, which indicates the potential lattice suitability of Sn atoms in perovskites. In addition, phonon DOS and vibration modes were also theoretically computed and visualized to offer a more effective perspective of the analysis. Atomic contribution of phonon DOS shows that Cs atoms mainly dominate the acoustic phonon branches, while B-site metal and halogen atoms occupy the main optical phonon branches. Pb-Sn substitution was confirmed to reduce the phonon bandgap and improve the potential up or down conversion of phonons. Phonon DOS with different optimization accuracy of Sn-based perovskites were compared and the lattice volume variation correlates well with their differences. The lattice structural information with different accuracy was separately given in Table S1. Computed vibration modes further demonstrated that the metal-halogen octahedrons possess the main vibration sources of perovskites, especially the low-frequency optical phonon branches.

2.1 | Electronic properties

The energy band structure is responsible for a wide range of physical characteristics observed in semiconductors, such as conductivity and light absorption. In this perspective, the electronic nature of perovskites is effectively described by their energy band structure and DOS. Recently, increasing research attempts are made to realize the bandgap engineering of perovskites by altering lattice compositions.[41,42] Without destroying the primary perovskite lattice structure, scholars selectively replace the metal and halogen atoms to further improve the environmental suitability of the bandgap. Notably, B-site metal and halogen elements in the same main group were frequently selected for substitution or doping to achieve energy band structure modulation because of their similar outermost electron distribution.[22,43] Here, we first simulate the energy band structures to elucidate primary physical principles in different substitution conditions. In Figure 1A–D, the energy band structure diagrams of $CsPbBr_3$, $CsPbI_3$, $CsSnBr_3$ and $CsSnI_3$ were listed in order. It is worth emphasizing that all the above perovskites are selected as cubic phases in order to seek a more concise and unified analysis. For every diagram, the orange dots (Alpha) and pure curves (Beta) represent the energy situations for different electron spin states, respectively. The good overlapping performance of Alpha and Beta curves indicates the extremely weak spin effect as well as the magnetic effect inside of these perovskites. Non-spin-polarized state shows that the spin density is zero inside of these perovskites, which describes their chemical stability. The regions separated by the vertical gray lines correspond to the areas between different symmetry points in the reciprocal space. The double-headed arrows were specially set to emphasize the calculated band gaps of these inorganic perovskites. Notably, $CsPbBr_3$, $CsPbI_3$, $CsSnBr_3$ and $CsSnI_3$ were all observed to have a direct bandgap at the R symmetry point and their corresponding bandgaps were calculated as 1.78, 1.463, 0.616 and 0.419 eV, respectively. Due to the instability of cubic phase inorganic halide perovskites at room temperature, little experimental band gap information can be found to make a convincing systematic comparison. In this work, these fundamental bandgap values along with the theoretical results from some other studies are presented in Table 1 for comparison, which provides effective evidence for the validity of our computation method and results because of the high numerical uniformity. As shown in Figure 1, these four inorganic perovskites maintain similar energy band structures at some high symmetry points such as G and R. However, the bandgap values of these perovskites were observed to have a distinguishable shrink after the Br-I substitution. A similar decrease of bandgap values also appears in lead halide chemicals after the introduction of heavier halogen atoms (Figure S1). This variation demonstrates the similar influence of halogen atoms on the electronic structures of these materials, despite their different lattice structures. In addition, Pb-Sn substitution can further induce a significant decline of the bandgap values. These intriguing phenomena indicate that

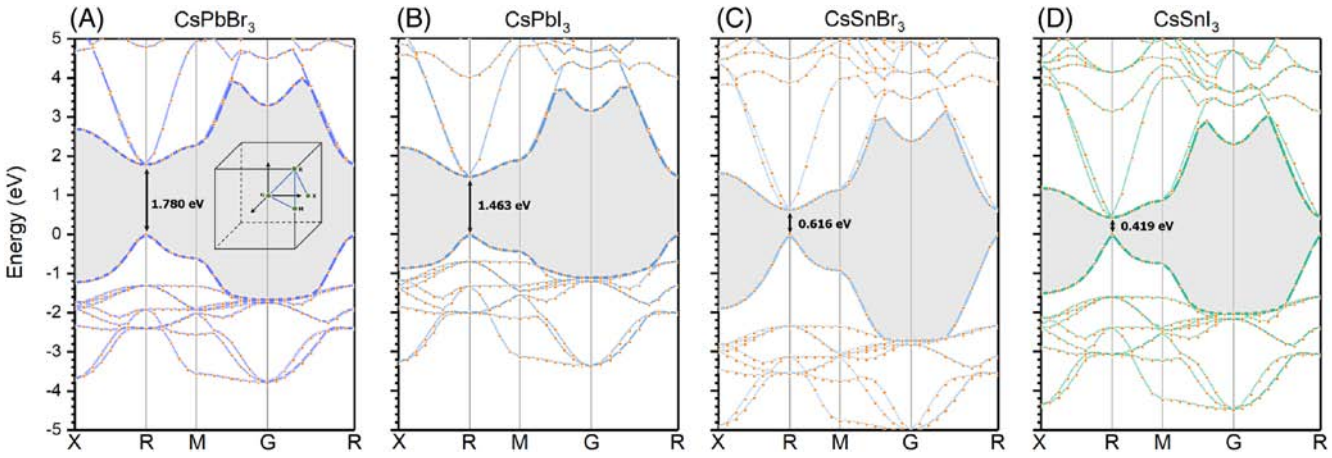

FIGURE 1 The computed band structure of cubic phase (A) $CsPbBr_3$, (B) $CsPbI_3$, (C) $CsSnBr_3$ and (D) $CsSnI_3$. The double-headed arrows illustrate the bandgap values. Orange dots represent the alpha curves. The inset cubic structure in (A) shows the first Brillouin zone and the corresponding calculated path of these materials

TABLE 1 The bandgap value comparison of cubic phase $CsPbBr_3$, $CsPbI_3$, $CsSnBr_3$ and $CsSnI_3$ between this work and other works

	Bandgap value	
Crystal	**This work**	**Other works**
$CsPbBr_3$	1.780 eV	1.760 eV[44], 1.663 eV[43]
$CsPbI_3$	1.463 eV	1.480 eV[45], 1.720 eV[19]
$CsSnBr_3$	0.616 eV	0.580 eV[46], 0.420 eV[47]
$CsSnI_3$	0.419 eV	0.434 eV[48], 0.462 eV[25]

the bandgap value was inherently related to the nature of the atomic energy level. To investigate the inner atomic mechanism of these bandgap value variations, we proposed the DOS diagrams of these perovskites.

In Figure 2A–D, the atomic contribution of the DOS and the energy positions with respect to Fermi level (E_F) were presented. By comparing the DOS curves, we noticed that the topmost valence bands of these perovskites are mainly occupied by the *p* orbitals of halogen atoms. Meanwhile, the DOS at the bottom of the conduction band is mainly dominated by the *p* orbitals of Pb or Sn, respectively. It is worth emphasizing that the simulated DOS curves of Br and I in Figure 2 only describe the contribution of one single atom, while each of the cubic perovskite lattices contains three halogen atoms. The results show that the Cs orbitals contribute little to the DOS no matter at the valence band top or conduction band bottom. Actually, the central large organic cations were also reported to have limited contribution to the bandgap values even in organic perovskites and only interact with the inorganic metal-halogen octahedra in the form of hydrogen bonds.[14] Another issue to discuss in this section is the intriguing energy band offset. Notably, the energy positions of the valence band top and conduction band bottom start to move towards E_F after the Br-I substitution. These energy band movements decrease the energy differences between the valence band top and conduction band bottom, which are responsible for the shrink of bandgap values. Besides, the Pb-Sn substitution induces the shifts of valence band top and conduction band bottom. Although the bottom of the conduction band still shifts towards E_F after Pb-Sn substitution, the top of the valence band starts to move away from E_F. In fact, the energy level of corresponding atomic orbitals correlates with these energy band offsets. Both Br and I are elements of the *VIIA* group, therefore sharing similar electronic properties. However, the outmost valence electrons of I are more prone to be excited to conduction band than Br due to its larger atomic radius. The energy position of I-*5p* is thus closer to E_F than Br-*4p*, which matches well with the shifting of valence band top induced by Br-I substitution. A similar concept is also adapted to explain the conduction band bottom offset induced by Pb-Sn substitution. Nevertheless, it is observed that the Br-I substitution induces the energy decline of the conduction band bottom, which is even predominated by the Pb or Sn orbitals. The valence band top, which is predominated by Br or I orbitals, also shifts after Pb-Sn substitution. Besides the energy, the band offset performance can be concluded that when the radius of the substituted atom increases, the bandgap-related orbitals (conduction band bottom or valence band top) of its bonded atom tend to approach E_F and vice versa. These intriguing features of the energy band offset reflect that the band structure of these inorganic perovskites is not only determined by the atomic orbital composition but also affected by the bonding properties.

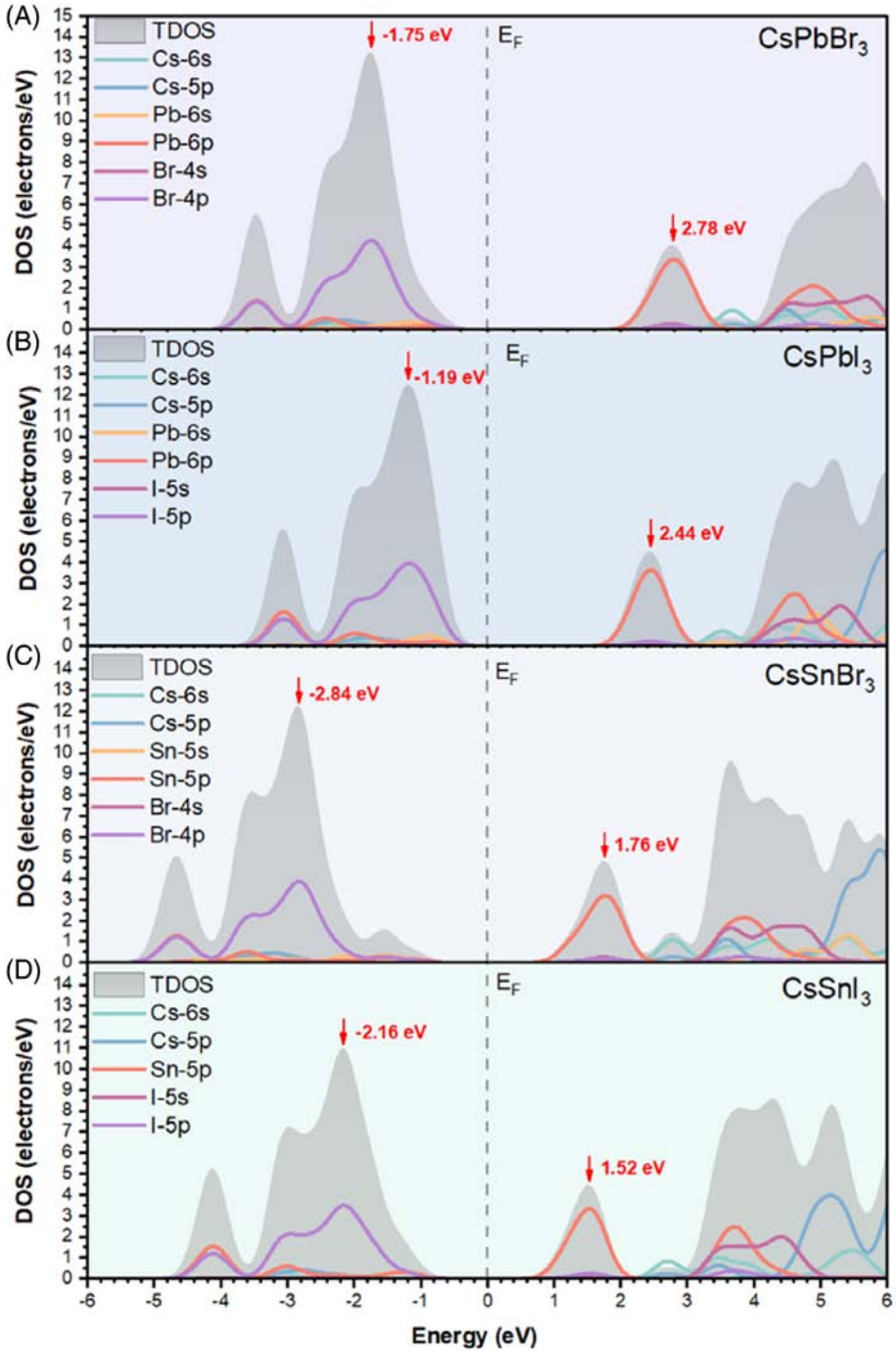

FIGURE 2 The calculated total and partial density of states (DOS) of cubic phase (A) $CsPbBr_3$, (B) $CsPbI_3$, (C) $CsSnBr_3$ and (D) $CsSnI_3$. The vertical dashed line represents the Fermi level. The gray area represents the total DOS and the colorful lines represent different atomic orbital contributions

Calculated electron density difference for cubic $CsPbBr_3$, $CsPbI_3$, $CsSnBr_3$ and $CsSnI_3$ are visualized in Figure 3. The electron density difference value comes from the difference between the molecular electronic density and the superimposed densities of the constituent non-interacting atoms, which was used to describe the electron redistribution upon molecule formation.[49] As we can distinguish, the variation of electron density indicates a strong covalent bond effect between the B-site metal and halogen atoms. These bonds were polarized, while the covalent electron pairs tend to approach the more electronegative atoms. Compared with Br, I atoms are less electronegative and thus show a weak ability to attract the covalent electron pairs. For a stationary B-site metal atom, the Br-I substitution will cause the movement of bonding electrons towards this B-site metal atom and thus induce a slight energy decrease of its valence orbitals. This matches well with the energy offsets of the conduction band bottom as observed in Figure 2. Similarly, the Pb-Sn substitution will reduce the bond length and make the valence orbitals of halogen atoms move away from E_F. Even though the energy level of atomic

orbitals is mainly determined by the atom itself, the interactions between atoms still need to be considered. The shrink of lattice volume facilitates the interaction between B-site metal and halogen atoms (see Table S2), which contributes to the observed features of energy band offsets. In addition, the calculated atomic populations of these four inorganic perovskites were further collected as listed in Table 2. To tackle the delocalized nature of the basis functions and perform the atomic population analysis,[22] the plane wave states were projected onto a localized basis using the technique proposed by Sanchez-Portal et al. and Mulliken.[50,51] As shown in Table 2, these four perovskites can be regarded as covalent compounds because of their modest charge differences. The charge of the most ionic Cs atom is only +0.57, which is obviously lower than its formal charge +1, indicating the possible covalent bonding mechanism of the Cs atom. Besides, there is a peculiar phenomenon that the charge of the Sn in cubic $CsSnI_3$ was discovered to be negative in the chemical environment produced by I ions, which may be attributed to the strong ability of Sn to attract the bonding electrons. However, the detailed bonding characteristics of these perovskites seem to be too complicated to completely explain only considering the fundamental electronegativity properties of these atoms. More profound theories need to be proposed to better confirm or predict the variation trend of the band structure of perovskites, which is out of the scope of this work.

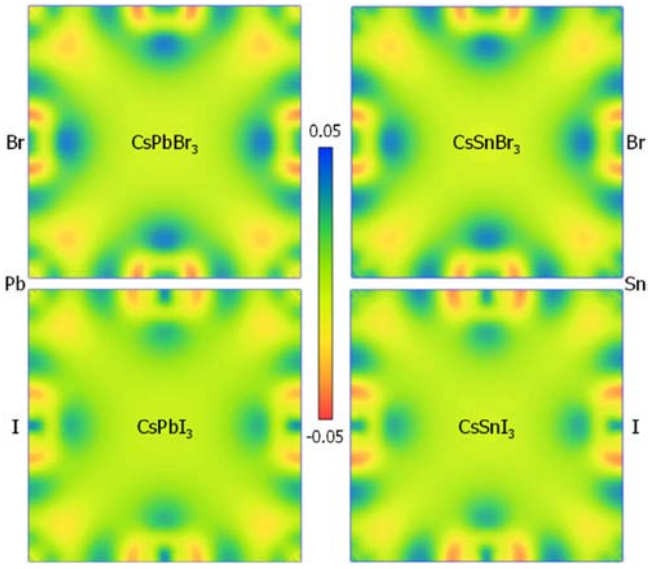

FIGURE 3 The (0 0 1) cross-sections of the computed electron density difference for cubic $CsPbBr_3$, $CsPbI_3$, $CsSnBr_3$ and $CsSnI_3$, respectively. The midpoints of all side lengths, as labeled, were occupied by halogen atoms, while the corners represent the B-site metal atoms. Cs atoms were not included for a brief comparison. The acquisition and loss of electrons are represented by the blue and red colors, respectively

2.2 | Optical properties

The optical properties of perovskites describe their response to the incident light of different frequencies. In nature, the interactions between the incident light and materials such as the light absorption and refraction can be attributed to the coupling of photons and internal electronic structure. By applying different atomic substitution conditions, the details of optical properties variation are revealed to guide the functional perovskites design. The optical properties of cubic $CsPbBr_3$, $CsPbI_3$, $CsSnBr_3$, and $CsSnI_3$ are of great importance and thus discussed in this work to further explore their

TABLE 2 The calculated atomic populations of cubic phase $CsPbBr_3$, $CsPbI_3$, $CsSnBr_3$ and $CsSnI_3$

Crystal	Atom	*s*	*p*	*d*	*f*	Total	Charge [*e*]
$CsPbBr_3$	Cs	2.18	6.35	0.00	0.00	8.54	0.46
	Pb	4.33	7.54	10.00	0.00	21.86	0.14
	Br	1.73	5.47	0.00	0.00	7.20	−0.20
$CsPbI_3$	Cs	2.20	6.31	0.00	0.00	8.51	0.49
	Pb	3.91	7.77	10.00	0.00	21.69	0.31
	I	1.86	5.40	0.00	0.00	7.27	−0.27
$CsSnBr_3$	Cs	2.19	6.37	0.00	0.00	8.56	0.44
	Sn	1.97	1.57	10.00	0.00	13.54	0.46
	Br	1.82	5.47	0.00	0.00	7.30	−0.30
$CsSnI_3$	Cs	2.20	6.23	0.00	0.00	8.43	0.57
	Sn	2.39	1.92	10.00	0.00	14.31	−0.31
	I	1.72	5.37	0.00	0.00	7.09	−0.09

relationships with the electronic structures. The complex dielectric function $\varepsilon(\omega)$ opens, which is thought to be able to reflect key information of the interaction between the photons and electrons, plays an important role in describing the linear response of the materials to electromagnetic radiation.[24,52] As expressed in Equation 1, the dielectric function $\varepsilon(\omega)$ consists of the real part $\varepsilon_1(\omega)$ and the imaginary part $\varepsilon_2(\omega)$. These two parts are not independent but follow the Kramer-Kronig relationship (see Supporting Information).[53] In fact, the response of a medium to an applied electric field is not instantaneous but delayed with some phase difference, which is in accordance with the law of causality. Therefore, the real part mainly demonstrates the phase modulation capability of the medium while the imaginary part describes the loss.

$$\varepsilon(\omega) = \varepsilon_1(\omega) + i\varepsilon_2(\omega) \tag{1}$$

As shown in Figure 4, we calculated the complex dielectric function of these four cubic perovskites in this work to explore their intriguing optical properties. The calculation process was based on the effective energy distribution of identical samples to support the accuracy. In Figure 4A, the solid curves represent the result of the real part $\varepsilon_1(\omega)$, which correspond to the left and bottom axes. The dashed curves represent the imaginary part $\varepsilon_2(\omega)$ and correspond to the right and top axes. The color of cyan, orange, red and blue represent cubic $CsPbBr_3$, $CsPbI_3$, $CsSnBr_3$ and $CsSnI_3$, respectively. Two black panes are used to label the first-peak regions of the real part $\varepsilon_1(\omega)$ and the imaginary part $\varepsilon_2(\omega)$, which are magnified displayed in Figure 4B,D, respectively. The olive arrows inside represent the corresponding atom substitution process. For the real part $\varepsilon_1(\omega)$ of the dielectric function of these four perovskites, the calculated curves keep a similar trend in general. They rise rapidly at first and then

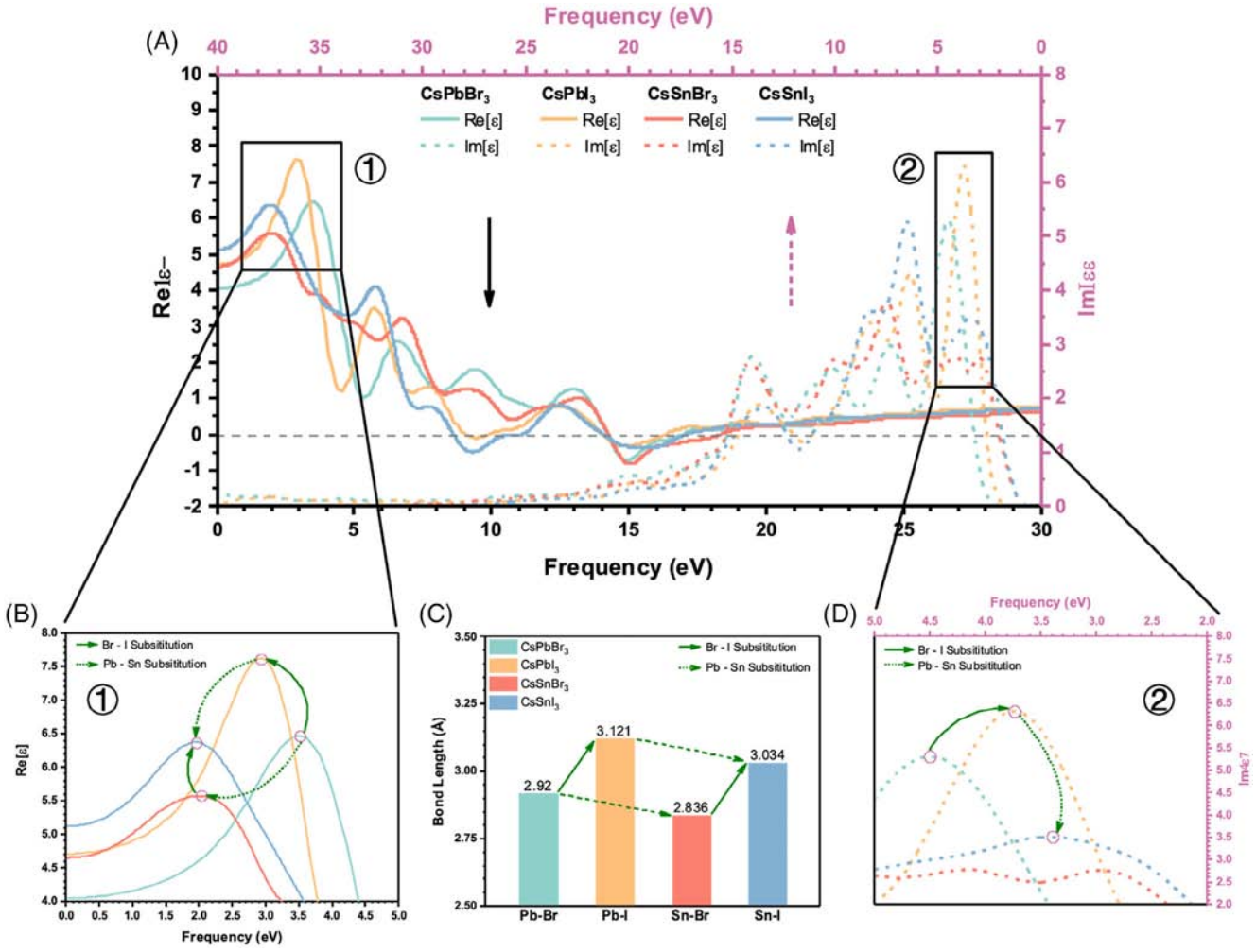

FIGURE 4 The calculated (A) complex dielectric function and the atom substitution influence on the (B) real part, (C) bond length and (D) imaginary part of cubic $CsPbBr_3$, $CsPbI_3$, $CsSnBr_3$ and $CsSnI_3$. The first peak of cubic $CsSnBr_3$ in (d) is not obvious enough and thus not marked

decline with fluctuations after reaching the maximum, and finally stabilize smoothly above zero. Some negative values of $\varepsilon_1(\omega)$ are found around 9 and 15 eV, which were also observed in some metallic materials with plasmon resonance.[54] The values of the real part $\varepsilon_1(\omega)$ at infinite wavelength of cubic $CsPbBr_3$, $CsPbI_3$, $CsSnBr_3$ and $CsSnI_3$ are calculated as 4.05, 4.71, 4.65 and 5.12, respectively. Essentially, these quantities are equal to the square of their corresponding refractive index. Besides, the first peaks of these curves are mainly located within the energy range of visible light. They were labeled by the black pane and displayed in Figure 4B. The exact peak positions of cubic $CsPbBr_3$, $CsPbI_3$, $CsSnBr_3$ and $CsSnI_3$ are calculated as 3.46, 2.95, 2.01 and 1.95 eV, respectively. Intriguingly, the $\varepsilon_1(0)$ values, as well as the peak position, will be regularly affected by the atomic substitution. When the Br atoms were replaced by the I atoms, the $\varepsilon_1(0)$ values tend to increase, and the peak positions slightly move to the low energy side. The Pb-Sn substitution will also induce the considerable redshift of peak positions as well as the decreased $\varepsilon_1(0)$ values. Characteristics of the peak positions match well with the mentioned band gap variation features of these perovskites, which shows the further connection between their electronic structures and optical properties. Meanwhile, as shown in Figure 4B,C, the offset of peak values induced by atomic substitution follows the variation of the bond length. When the bond length was elongated due to the Br-I substitution, these peak positions tend to move towards the lower energy side, no matter the real or imaginary part. This feature is consistent with the trend of bandgap reduction induced by the Br-I substitution, which indicates the lower threshold of optical response in I-based perovskites. The peak values, however, show a slight enhancement after the Br-I substitution and thus represent a stronger optical response. In the case of Pb-Sn substitution, the peak positions shift to the lower energy side, while the peak values decrease. It can be concluded that the energy positions of the above peaks are determined by the atomic compositions, while the values are affected by the bond length. This parallelogram-like relationship implies that the bonding properties can not only influence the bandgap shifting but also the dielectric response, which may be further applied to optimize the optoelectronic characteristics of functional devices.

The imaginary part $\varepsilon_2(\omega)$ of the dielectric function of these perovskites, as shown in Figure 4A, display a sharp increase at first. The corresponding critical points of $CsPbBr_3$, $CsPbI_3$, $CsSnBr_3$ and $CsSnI_3$ are calculated as 1.98, 1.56, 0.46 and 0.42 eV, respectively. The ordering of these values was consistent well with the bandgap size. Besides, the first peaks also share a similar relationship between the peak characteristics and atomic substitution conditions as discussed in $\varepsilon_1(\omega)$ part, which is especially demonstrated in Figure 4D. In detail, both Br-I substitution and Pb-Sn substitution will induce the redshift of peak positions. However, Br-I substitution will result in the enhancement of peak values, while Pb-Sn substitution will decline the peak values. Except for the discussed first peak regions, other energy ranges of the complex dielectric function are also regularly affected by different atomic compositions. For example, Br-based perovskites show a higher intensity of real and imaginary parts of complex dielectric function around 10 eV than I-based perovskites. Derived from the different electronic structures induced by various atomic compositions, these diverse dielectric function responses in specific energy ranges can be utilized to fabricate functional devices such as optical filters.

According to the obtained complex dielectric function, we further calculated the results of the refractive index of these four perovskites (Figure S3), which are listed in Figure 5A. In detail, the $n(0)$ values of $CsPbBr_3$, $CsPbI_3$, $CsSnBr_3$ and $CsSnI_3$ are calculated as 2.01, 2.17, 2.16 and 2.26, respectively. Clearly, the refractive indices of these materials process a sharp rise from the infinite wavelength limits and then reach the corresponding maximum values, which are calculated as 2.59, 2.82, 2.38, and 2.54, respectively. Derived from the dielectric function, these results match well with the bonding features as shown in Figure 4C. At higher frequencies, the refractive indices of these materials tend to decline in general. Their values are even less than one in certain energy ranges, which represents the extreme phase velocity of the corresponding incident radiation.[24] These intriguing near-zero refractive indices demonstrate that perovskites have the potential to be further applied in tailoring the radiation phase pattern or waveguiding.[55,56] For the extinction coefficient in Figure 5A, it seems that Pb and Sn-based perovskites show different peak energy regions (ca. 5 eV for Pb-based perovskites and ca. 8 eV for Sn-based perovskites). This indicates that the enhancement of the light absorption ability of perovskites at certain frequencies can be realized by selective doping of Pb or Sn atoms. Besides, the start and endpoints of the imaginary part $k(\omega)$ of $CsPbBr_3$, $CsPbI_3$, $CsSnBr_3$ and $CsSnI_3$ are same as the results of $\varepsilon_2(\omega)$, which is theoretically verified by Equation S5. Moreover, the complex optical conductivity $\sigma(\omega)$, plotted in Figure 5B, can be derived from the acquired dielectric function $\varepsilon(\omega)$ as shown in Equation 2, where ε_0 represents the vacuum permittivity.

$$\varepsilon(\omega) = \varepsilon_0 + \frac{i\sigma(\omega)}{\omega} \tag{2}$$

In fact, the optical conductivity $\sigma(\omega)$ describes the ability of semiconductors to change the conductivity in response

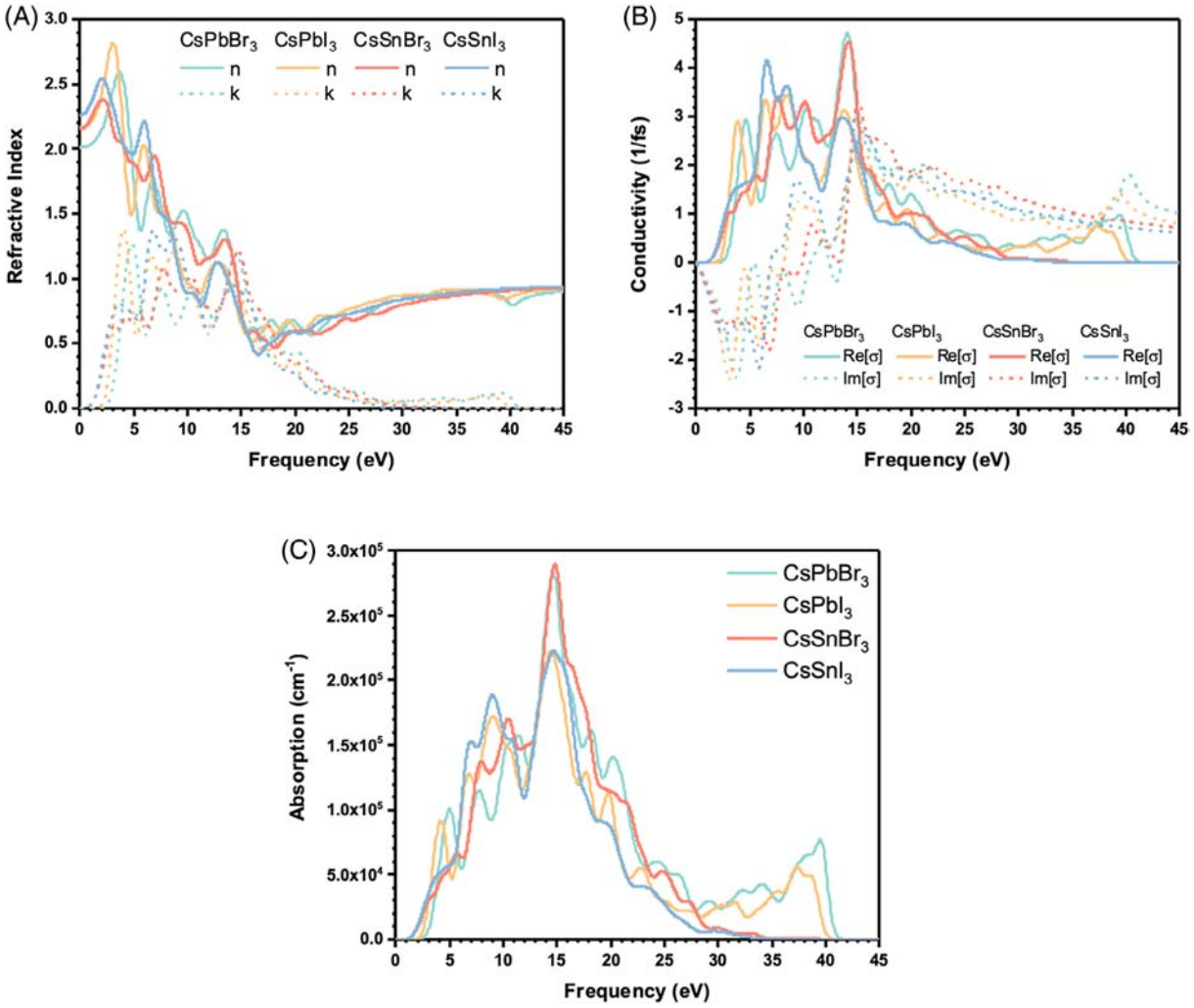

FIGURE 5 Calculated (A) complex refractive index, (B) complex optical conductivity, (C) absorption coefficient of cubic $CsPbBr_3$, $CsPbI_3$, $CsSnBr_3$ and $CsSnI_3$

to light radiation, which is useful in optoelectronic areas such as radiation detection.[57,58] The real part of $\sigma(\omega)$ is closely related to the extinction coefficient, which can be verified by the similar peak features between the real part of $\sigma(\omega)$ and $k(\omega)$ as shown in Figure 5A,B. The maximum values of conductivity of cubic $CsPbBr_3$, $CsPbI_3$, $CsSnBr_3$ and $CsSnI_3$ are calculated as 4.714 fs^{-1} (at 14.1 eV), 3.445 fs^{-1} (at 8.42 eV), 4.544 fs^{-1} (at 14.19 eV) and 4.169 fs^{-1} (at 6.58 eV), respectively. Besides, the imaginary part of $\sigma(\omega)$ has a similar fluctuation trend as $\varepsilon_1(\omega)$. Their relationship allows scholars to selectively work out the conductivity or dielectric function according to the specific type of materials.[59] The absorption coefficient $\alpha(\omega)$ of medium is derived from the corresponding extinction coefficient $k(\omega)$ as shown in Equation 3, where c represents the speed of light.

$$\alpha(\omega) = \frac{2\omega k(\omega)}{c} \tag{3}$$

The calculated absorption coefficient $\alpha(\omega)$ of the four perovskites are plotted in Figure 5C. We observed that the Pb-based perovskites exhibit stronger absorption ability around 5 eV. This phenomenon is determined by the higher DOS of $CsPbBr_3$ and $CsPbI_3$ around 5 eV as shown in Figure 2. In addition, Pb-based perovskites also show considerable absorption even at a high energy range, 30–40 eV, which is almost transparent to $CsSnBr_3$ and $CsSnI_3$. This finding reveals the absorption deficiency of Sn-based perovskites in the high energy range and can be further applied to the detection of Sn atoms in perovskites. The maximum absorption coefficient of cubic $CsPbBr_3$, $CsPbI_3$, $CsSnBr_3$ and $CsSnI_3$ are computed as 2.83×10^5 cm^{-1} (at 14.70 eV), 2.23×10^5 cm^{-1}

(at 14.45 eV), 2.89×10^5 cm^{-1} (at 14.82 eV) and 2.22×10^5 cm^{-1} (at 14.70 eV), respectively. Notably, the energy positions of these peaks are similar, although the values of the maximum absorption coefficient are influenced by the halogen atoms. Br-based perovskites are confirmed to demonstrate higher absorption than I-based cases when the incident light is around 15 eV. All above results illustrate that the atomic substitution will regularly affect the optical properties of perovskites and the methodology in our work provides an effective prediction for perovskite modification engineering.

2.3 | Vibrational properties

In this work, we further calculated and analyzed the vibrational properties of cubic $CsPbBr_3$, $CsPbI_3$, $CsSnBr_3$ and $CsSnI_3$. The obtained phonon dispersion spectra of these four inorganic perovskites as well as their corresponding phonon DOS were demonstrated in Figure 6 in order. Different from the complex phonon structure of organic perovskites,[60] the calculated phonon states in this work are mainly concentrated in the low energy range (−30 to 180 cm^{-1}) including acoustic phonon branches and low-frequency optical phonon branches. The performance of the computed phonon properties of these four perovskites in this work keeps in line well with some previous studies,[29,61–63] which confirms the validity of the calculation approaches and corresponding results. In detail, it was distinguished that some imaginary frequency curves exist in our computed phonon dispersion diagrams. These unexpected imaginary frequency curves are active in not only our results but also other studies,[29,61–63] which usually implies the potential structural instability in the materials. However, our results show that the imaginary frequency phonon states can be greatly reduced and even vanish after the Pb-Sn substitution. This indicates that the Pb-Sn substitution has a relevant "repairing effect" on the intrinsic permanent displacement of atoms, which is induced by the distortion of the metastable lattice of perovskite materials.[31] In Figure 6A, it can be observed that the three labeled peaks of the phonon DOS, 21.75, 59.61 and 156.52 cm^{-1}, are mainly dominated by Cs, Br and Pb atom, respectively. There are totally three Br atoms in one cubic lattice, which means the 59.61 cm^{-1} peak was almost entirely occupied by the Br composition. Similar peak characteristics were found in cubic $CsPbI_3$, despite

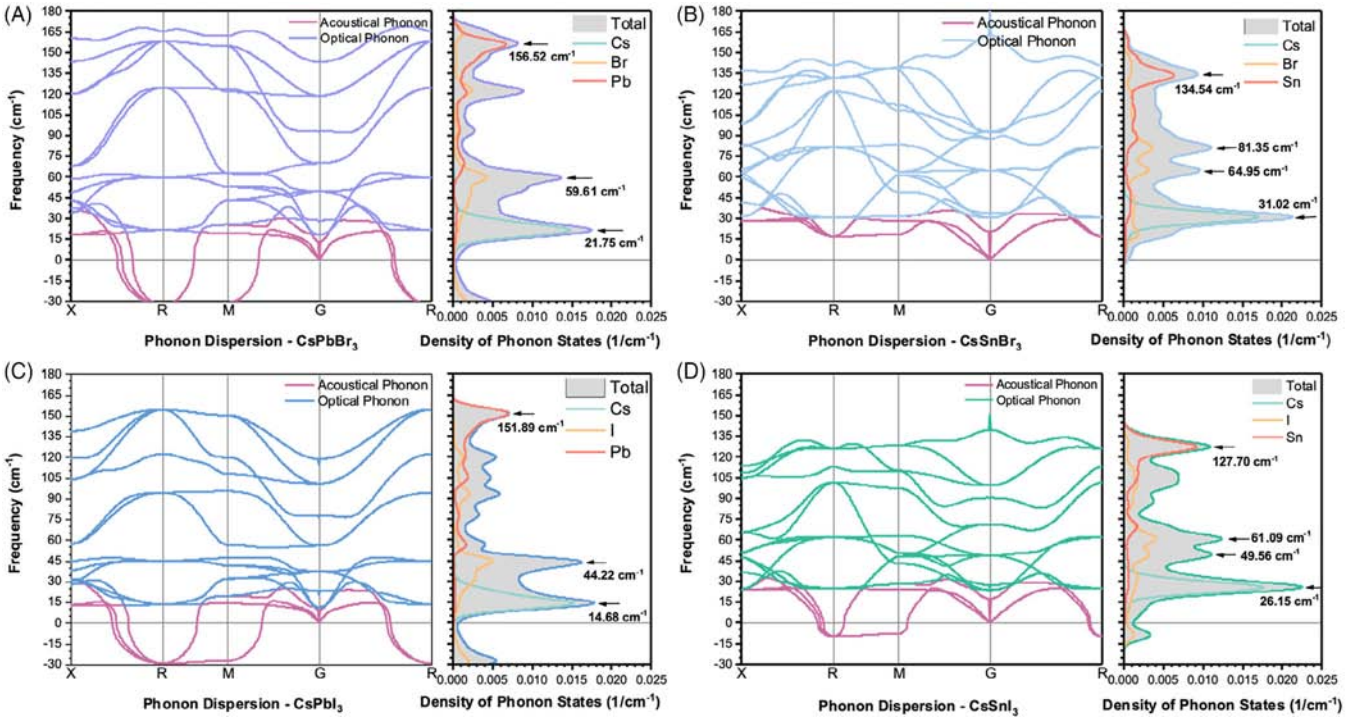

FIGURE 6 The calculated phonon dispersion spectrum and the corresponding phonon density of states (DOS) of cubic (A) $CsPbBr_3$, (B) $CsPbI_3$, (C) $CsSnBr_3$ and (D) $CsSnI_3$, respectively. The curves of the acoustical phonon branch were specially set as purple color. In addition, the plots of the phonon DOS were deliberately placed vertically to match the energy position of the phonon dispersion curves on the left side. The gray area represents the total phonon DOS of the corresponding crystal lattice, while the other colorful lines describe different atomic contributions. The energy positions of some conspicuous peaks of the total phonon DOS were specially labeled for a brief comparison

the frequency positions of the three peaks having a slight decrease, labeled as 14.68, 44.22 and 151.89 cm^{-1}. Br-I substitution induced offset of energy positions for these main phonon state peaks also exists in the Sn-based perovskites as shown in Figure 6C,D. These intrinsic phonon properties associated with the halogen atoms provide effective information to further regulate the phonon band structure of perovskites.

Different from the Pb-based perovskites, $CsSnBr_3$ and $CsSnI_3$ demonstrate a more "concentrate" phonon DOS as presented in Figure 6C,D. The Cs dominated phonon states peak performs a slight blueshift, while the energy of the Sn dominated peak is obviously decreased. Notably, the observed single phonon peak occupied by the halogen atoms in Pb-based perovskites starts to split into two peaks after the Pb-Sn substitution. Meanwhile, the shrinking of the phonon range also appears in lead halide chemicals, as shown in Figure S2, after the substitution of halogen atoms. This common kind of concentrated phonon band structure introduces more overlapping phonon branches and thus concentrate more phonon states as shown in Figure 6 and Figure S2. Increased phonon DOS improves the phonon delocalization and helps to avoid the potential phonon bandgap. Therefore, the up or down conversion of different phonon modes in these perovskites can be enhanced to eliminate the hot-phonon bottleneck effect and improve lattice energy transfer.[31] In addition, the introduction of Sn atoms shows the ability to reduce the imaginary frequency part of phonon states, even though it is mainly dominated by halogen atoms. This intriguing phenomenon was determined by the interaction between B-site metal and halogen atoms, which is attributed to the high suitability of the metal-halide octahedron in Sn-based perovskites.

Kohn anomalies of these perovskites were also observed in their phonon dispersion curves near the Gamma point (Figure S4). The abrupt change of lattice vibration shielding by conduction electrons, as reported in previous studies, is mainly responsible for these unusual discontinuities and kinks.[64,65] In Pb-based perovskites, the energy levels of the associated phonons near the Gamma point are considerably lowered and companied with the softening trend of phonon branches. However, these originally sunken phonon branches start to become flat and even convex after the Pb-Sn substitution. The highest frequency optical branch in Sn-based perovskites even shows a peak-like convex discontinuity near Gamma point, which is the opposite of the Pb-based perovskites. This implies that the Pb-Sn substitution can hinder the phonon softening and change the vibration screening in perovskites. In addition, the variation of these Kohn anomalies provides effective evidence for the metallization tendency of these perovskites after the Pb-Sn substitution,[66] which has been discussed above.

Following the phonon analysis of these four perovskites, the influence of geometric optimization accuracy on the phonon DOS of Sn-based perovskites was demonstrated in Figure 7A,B. High geometric optimization accuracy improves the relaxation sensitivity of atoms subjected to strain in the lattice and thus increases the structural stability. As labeled by the left black arrow in Figure 7, the more relaxed structure maintained higher lattice stability and thus showed lower imaginary frequency parts. Notably, this feature matches well with the mentioned imaginary frequency decline, which was induced by Pb-Sn substitution, as shown in Figure 6. This result further verifies that the Pb-Sn substitution helps to improve the stability of cubic perovskite lattice by increasing the atomic relaxation. Meanwhile, the phonon DOS near 30 cm^{-1} was significantly increased with the improvement of lattice relaxation. The decrease of lattice volume, which was induced by enhancing geometric optimization accuracy, strengthens the influence of Cs atom on the surrounding metal-halogen octahedrons and finally increases the intensity of Cs-dominated phonon branches. The detailed lattice information with different geometric optimization accuracy was proposed in Tables S1 and S2.

Although phonon DOS and dispersion curves contribute to the investigation of the vibration distribution, they are not evident enough to clarify the vibration source of these inorganic perovskites. Vibration modes, which are used to describe the atomic relative motions in the lattice, can help us better understand the symmetry features and IR (or Raman) activity of the corresponding materials. The detailed results of the calculated vibrational modes and the assignation are presented in Table 3. In fact, each lattice of these four perovskites contains five atoms and 15 vibration modes in total as shown in Figure 6, including three acoustic branches and 12 optical branches. The structure of these cubic phase perovskites, belonging to the space group *Pm-3m* in the Hermann-Mauguin notation, can be understood as consisting of halogen ion angles shared by two metal-halogen octahedrons, with the Cs atom occupying the center of the cavity formed by the nearby eight octahedrons.[67] In detail, both of the Cs and Pb (or Sn) atoms occupy the O_h sites, each of which contributes T_{1u} symmetry mode, while the other three halogen atoms contribute with $2T_{1u} + T_{2u}$ modes.[68] Therefore, the sum symmetry modes at the center of the Brillouin zone are described as $\Gamma = 4T_{1u} + T_{2u}$. Factor group analysis[69] of cubic $CsPbBr_3$ can be found in Supporting Information. It is necessary to stress that there are no expected active vibrational Raman modes in the calculation results, which is attributed to the lack of

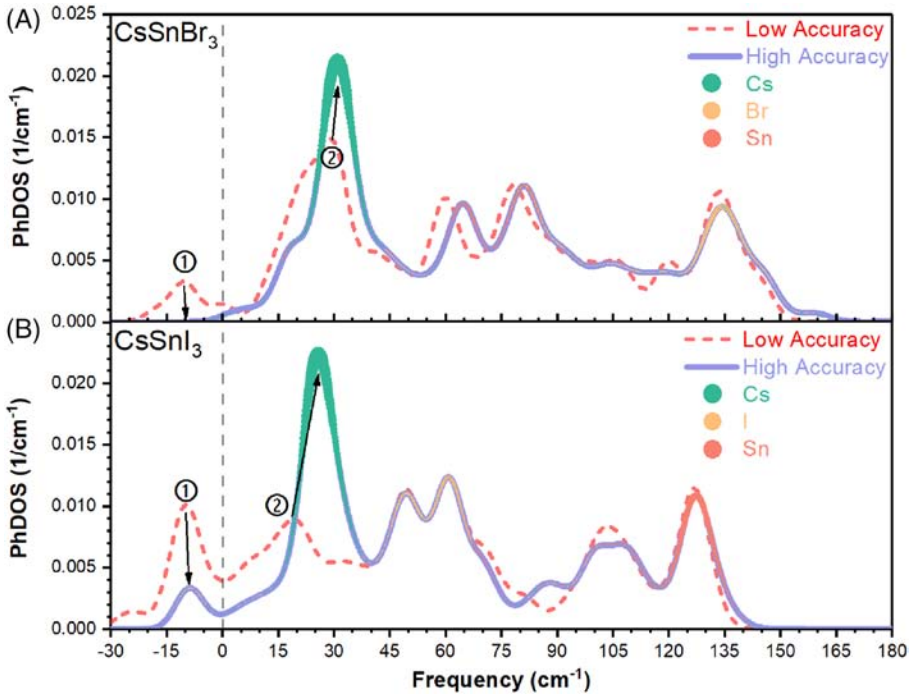

FIGURE 7 The phonon density of states (DOS) of cubic phase (A) $CsSnBr_3$ and (B) $CsSnI_3$ with low and high geometry optimization accuracy. Dashed and solid lines represent the calculated phonon DOS with low and high geometric optimization accuracy, respectively. The colorful bubbles represent the projection of the individual atomic contribution onto the total phonon DOS. The size and density of these bubbles roughly describe the corresponding contribution ratio. The black arrows as well as the nearby numbers label the two significant variations of the phonon DOS after improving the optimization accuracy

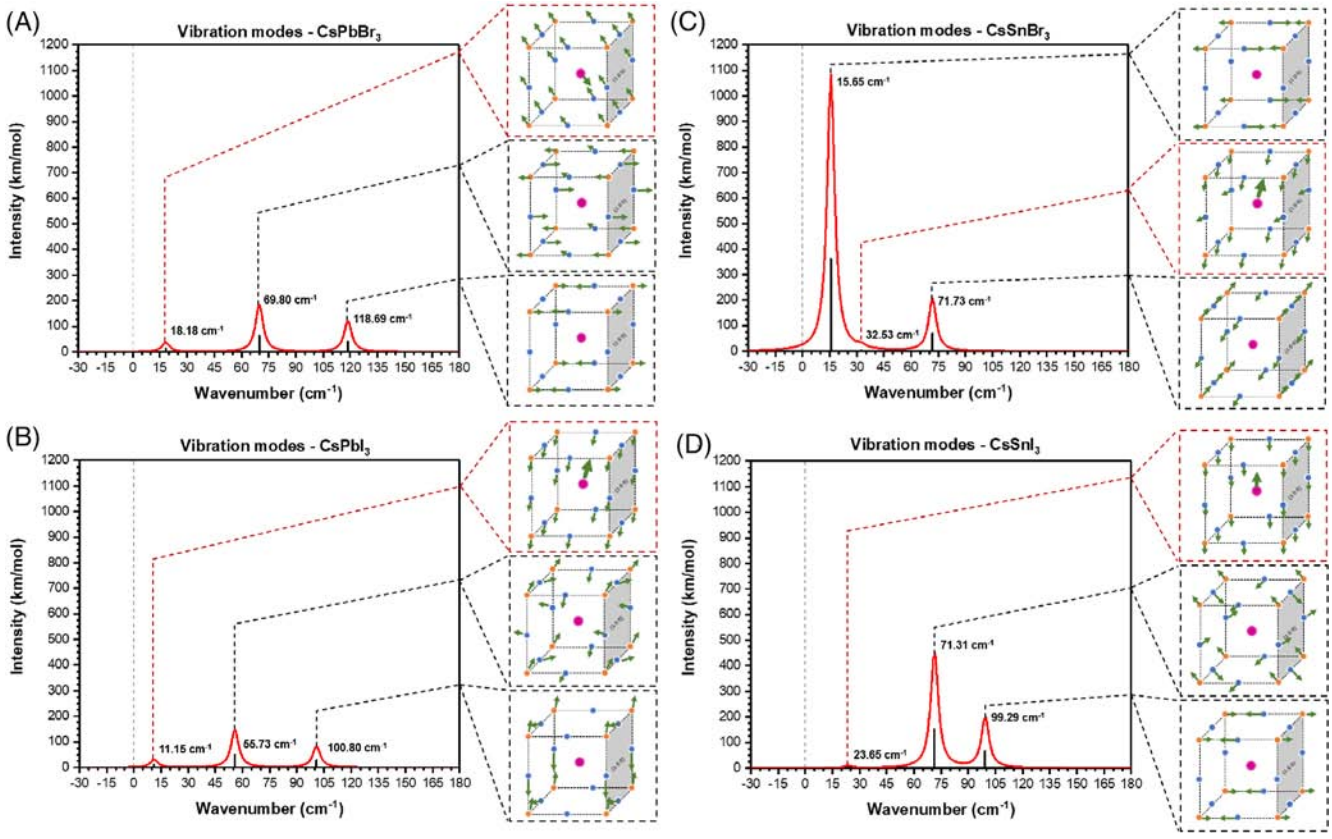

FIGURE 8 The simulated infrared spectrum and corresponding active vibration modes of cubic phase (A) $CsPbBr_3$, (B) $CsPbI_3$, (C) $CsSnBr_3$ and (D) $CsSnI_3$, respectively. The black lines mark the exact energy position of the corresponding vibration modes, which were specially visualized on the right side. The amaranth, orange, and navy spheres represent the Cs atom, B-site atoms, and halogen atoms, respectively. The olive arrows point out the vibrational directions of the connected atom and their size roughly describes the vibrational intensity. The gray plane on the right side was the labeled benchmark (1 0 0) plane. Cs-involved vibration modes were specially labeled with red panes

TABLE 3 The calculated vibrational modes and assignation of cubic $CsPbBr_3$, $CsPbI_3$, $CsSnBr_3$ and $CsSnI_3$

	$CsPbBr_3$		$CsPbI_3$		$CsSnBr_3$		$CsSnI_3$	
Mode number	**Wavenumber (cm^{-1})**	**Vibrational mode**	**Wavenumber (cm^{-1})**	**Vibrational mode**	**Wavenumber (cm^{-1})**	**Vibrational mode**	**Wavenumber (cm^{-1})**	**Vibrational mode**
1	−0.013	T_{1u}	−0.012	T_{1u}	−0.014	T_{1u}	−0.013	T_{1u}
2	−0.013		−0.012		−0.014		−0.013	
3	−0.013		−0.012		−0.014		−0.013	
4	18.221	T_{1u}	11.225	T_{1u}	15.640	T_{1u}	23.645	T_{1u}
5	18.221		11.225		15.640		23.645	
6	18.221		11.225		15.640		23.645	
7	49.465	T_{2u}	37.203	T_{2u}	32.522	T_{1u}	48.786	T_{2u}
8	49.465		37.203		32.522		48.786	
9	49.465		37.203		32.522		48.786	
10	69.780	T_{1u}	55.737	T_{1u}	48.951	T_{2u}	71.310	T_{1u}
11	69.780		55.737		48.951		71.310	
12	69.780		55.737		48.951		71.310	
13	118.674	T_{1u}	100.795	T_{1u}	71.730	T_{1u}	99.291	T_{1u}
14	118.674		100.795		71.730		99.291	
15	118.674		100.795		71.730		99.291	

quadratic functions of all T_{1u} and T_{2u} modes (see Table S3). These quadratic functions represent the induced polarizability of the symmetry species, which is the prerequisite for a chemical to be Raman active. However, all T_{1u} modes are supposed to be infrared active because their eigenmodes belong to one of the irreducible representations of the electric dipole operator.[60] The linear functions of these irreducible representations relate to the translational movements of the atoms and thus represent the potential dipole moment. One acoustic branch T_{1u} mode was calculated to be located at the imaginary frequency part as shown in Table 3 and thus not displayed in our visualized infrared spectrums.

Based on the computed data of vibration modes, we then simulated the infrared spectrum of the four perovskites and visualized the related active atomic motions as shown in Figure 8. For cubic $CsPbBr_3$, three main vibration modes were observed as 18.18, 69.80 and 118.69 cm^{-1} (Figure 8A). As we can see, the weak 18.18 cm^{-1} vibration mode mainly describes the relative motion between the Cs atom and the whole lattice, which is located at the low-frequency phonon range. Besides, the 69.80 and 118.69 cm^{-1} vibration modes mainly describe the interlayer and adjacent vibration of the Pb-Br octahedrons, respectively. As shown in Figure 8B, the wavenumber of the three vibration modes of $CsPbI_3$ was observed as 11.15, 55.73 and 100.80 cm^{-1}, respectively. The energy positions of these vibration modes match well with those of cubic $CsPbBr_3$. Despite there are some slight redshifts, they also maintain similar intensity. The visualized vibration modes also demonstrate the similar vibration characteristics of cubic $CsPbBr_3$, which means that the interlayer and adjacent relative motion of Pb-halogen octahedrons provide the main vibration source. For cubic $CsSnBr_3$, the three main energy positions of the vibration modes in Figure 8C were detected as 15.65, 32.53 and 71.73 cm^{-1}, respectively. The 15.65 cm^{-1} vibration mode, which describes the stretching motion between the adjacent Sn-Br octahedrons, exhibits extremely strong intensity. However, the 32.53 cm^{-1} vibration mode, which is contributed by Cs atoms, shows negligible intensity. Strong vibration intensity represents a larger vibrational dipole moment in this mode, which is attributed to the unique orbital distribution as well as the bonding properties of the Sn-Br octahedrons. On the contrary, as shown in Figure 8D, the calculated vibration modes of cubic $CsSnI_3$ maintain a high consistency with cubic $CsPbI_3$ rather than $CsSnBr_3$. The 23.65 cm^{-1} mode performs a negligible vibration intensity while the 71.31 and 99.29 cm^{-1} modes remain active with considerable intensity.

In general, the assignation of these infrared spectrum peaks, which was illustrated in Figure 8, corresponds to three vibration cases: relative motion between Cs atom and octahedrons, tilting between different octahedron arrays, and stretching between adjacent octahedrons. Different atomic substitution conditions also have an influence on the offsets of these peaks as well as their intensity. The frequencies of the Cs-involved vibration modes were calculated as 18.18, 11.15, 32.53 and 23.65 cm^{-1} for cubic $CsPbBr_3$, $CsPbI_3$, $CsSnBr_3$ and $CsSnI_3$, respectively. Notably, the intensities of these vibration modes are negligible, even though Cs atoms are located at the center of the lattice cavity. This illustrates that the octahedrons composed of B-site metal atoms and halogen atoms are the main source for perovskites to provide vibration modes to couple with their electronic structures. In addition, even the symmetry conditions of Cs atoms will change in different structure phases of Cs-based perovskites, they still do not evidently contribute to the high-intensity vibration modes.[60] Tilting between octahedron arrays demonstrated higher frequencies. We calculated the frequencies of these vibration modes as 69.80, 55.73, 71.73 and 71.31 cm^{-1}, for cubic $CsPbBr_3$, $CsPbI_3$, $CsSnBr_3$ and $CsSnI_3$, respectively. The Br-I substitution is confirmed to induce a slight redshift of these peaks while Pb-Sn substitution does the opposite. Although atomic substitutions have limited influence on the shear motions of different octahedron arrays, they still show the potential to trigger phase transition of perovskites materials by modulating the vibration of their octahedron frame.[70] Another intriguing vibration feature to discuss is the stretching between the adjacent octahedrons. The frequencies of these modes were calculated as 118.69, 100.80, 15.65 and 99.29 cm^{-1}, for cubic $CsPbBr_3$, $CsPbI_3$, $CsSnBr_3$ and $CsSnI_3$, respectively. The stretching motion of cubic $CsSnBr_3$ demonstrates a low frequency but high-intensity peak in the simulated infrared spectrum, which may be attributed to the peculiar force constant of the Sn-Br bond. In addition, the Br-I substitution also shows the ability to induce a redshift of the stretching peak by comparing $CsPbBr_3$ and $CsPbI_3$. These atomic substitutions show direct influence on the dipole moments of corresponding bonds and eventually cause the peak offsets in the computed infrared spectra. These findings reveal the atomic contribution to the vibration modes of cubic inorganic perovskites and provide a new perspective to understand the relationship between perovskite lattice and phonon characteristics.

3 | CONCLUSION

In this work, we applied the density functional theory to calculate the electronic, optical, and vibrational properties of cubic inorganic perovskites $CsPbBr_3$, $CsPbI_3$,

$CsSnBr_3$ and $CsSnI_3$. We carried out the computed energy bandgap value of these perovskites as 1.78, 1.463, 0.616 and 0.419 eV, respectively. Diagrams of the total and partial DOS were proposed and analyzed. It was revealed that the conduction band bottom and valence band top are mainly contributed by the orbitals of B-site metal and halogen atoms, respectively. Therefore, bandgap engineering of perovskites may be more efficient when making the substitution of B-site metal or halogen atoms, rather than A-site cations. In addition, Pb-Sn substitution shows a stronger ability to adjust the bandgap based on the orbital energy offset than Br-I substitution. The change of bonding energy levels induced by the differences in bond length and atomic electronegativity are mainly responsible for the orbital energy offset. The optical properties of these four perovskites were further compared by analyzing the frequency-dependent complex dielectric function. Pb-Sn substitution induces the first peak decrease of dielectric function in the visible light range, while Br-I substitution causes the increase. These variations correlate well with bond length differences between B-site metal and halogen atoms. These computed results provide effective predictions for perovskite modification engineering. Phonon dispersion curves and the partial phonon DOS of these perovskites were also calculated together. The B-site metal atoms were verified to mainly contribute to some "middle" frequency phonon branches (around 40–90 cm^{-1}) and the Pb-Sn substitution will decline the potential phonon bandgap to improve the up or down conversion of phonons. This can be further applied to guide the elimination of the hot-phonon bottleneck effect in perovskites. Besides, the phonon DOS of Sn-based perovskites with different geometric optimization accuracy was compared. High optimization accuracy can reduce the imaginary frequencies and enhance the Cs-dominated phonon states. These results are attributed to the decreased but adaptive lattice volume. The detailed vibration modes assignation and relevant infrared spectrums were calculated and visualized. Cs-dominated vibration modes were verified to own little contribution and thus the adjacent and interlayer relative motions of the metal-halogen octahedrons were deemed to be the main vibration sources of perovskites. The theoretical analysis for these perovskites of great potential in our work can provide effective computed data to guide the exploration of their internal physical properties and offer a new perspective to further design more advanced materials.

ACKNOWLEDGMENTS

We gratefully acknowledge the financial support from the National Key R&D Program of China (2021YFA1501101), the NSFC/RGC Joint Research Scheme Project (N_PolyU502/21), the funding for Projects of Strategic Importance of the Hong Kong Polytechnic University (Project Code: 1-ZE2V), and the Collaborative PhD Training Programme by The Hong Kong Polytechnic University and Southern University of Science and Technology.

AUTHOR CONTRIBUTION

B. H. and R. C. conceived and led this project. B. C. carried out the theoretical calculations and data analysis. M. S. helped with the data analysis. All the authors contribute to the preparation of the manuscript.

CONFLICT OF INTEREST

The authors declare no conflict of interest.

ORCID

Rui Chen https://orcid.org/0000-0002-0445-7847
Bolong Huang https://orcid.org/0000-0002-2526-2002

REFERENCES

1. Stoumpos CC, Kanatzidis MG. The renaissance of halide perovskites and their evolution as emerging semiconductors. *Acc Chem Res*. 2015;48(10):2791-2802.
2. Akbulatov AF, Martynenko VM, Frolova LA, et al. Intrinsic thermal decomposition pathways of lead halide perovskites $APbX_3$. *Sol Energy Mater Sol Cells*. 2020;213(15):11559.
3. Usiobo OJ, Kanda H, Gratia P, et al. Nanoscale mass-spectrometry imaging of grain boundaries in perovskite semiconductors. *J Phys Chem C*. 2020;124(42):23230-23236.
4. Savenije TJ, Ponseca CS, Kunneman L, et al. Thermally activated exciton dissociation and recombination control the carrier dynamics in organometal halide perovskite. *J Phys Chem Lett*. 2014;5(13):2189-2194.
5. Wehrenfennig C, Eperon GE, Johnston MB, Snaith HJ, Herz LM. High charge carrier mobilities and lifetimes in organolead trihalide perovskites. *Adv Mater*. 2014;26(10):1584-1589.
6. Ponseca CS, Savenije TJ, Abdellah M, et al. Organometal halide perovskite solar cell materials rationalized: ultrafast charge generation, high and microsecond-long balanced mobilities, and slow recombination. *J Am Chem Soc*. 2014;136(14):5189-5192.
7. Stranks SD, Eperon GE, Grancini G, et al. Electron-hole diffusion lengths exceeding 1 micrometer in an organometal trihalide perovskite absorber. *Science*. 2013;342(6156):341-344.
8. A decade of perovskite photovoltaics. *Nat Energy*. 2019;4(1):1.
9. Mitzi DB, Field CA, Harrison WTA, Guloy AM. Conducting tin halides with a layered organic-based perovskite structure. *Nature*. 1994;369(6480):467-469.
10. Murtaza G, Ahmad L, Amin B, et al. Investigation of structural and optoelectronic properties of $BaThO_3$. *Opt Mater*. 2011;33(3):553-557.
11. Ning Z, Gong X, Comin R, et al. Quantum-dot-in-perovskite solids. *Nature*. 2015;523(7560):324-328.
12. Fu P, Hu S, Tang J, Xiao Z. Material exploration via designing spatial arrangement of octahedral units: a case study of lead halide perovskites. *Front Optoelectron*. 2021;14:252-259.
13. Thind A, Huang X, Sun J, Mishra R. First-principles prediction of a stable hexagonal phase of $CH_3NH_3PbI_3$. *Chem Mater*. 2017; 29:6003-6011.

14. Motta C, Mellouhi FE, Kais S, Tabet N, Alharbi F, Sanvito S. Revealing the role of organic cations in hybrid halide perovskite $CH_3NH_3PbI_3$. *Nat Commun*. 2015;6(1):7026.
15. Han D, Shi H, Ming W, et al. Unraveling luminescence mechanisms in zero-dimensional halide perovskites. *J Mater Chem C*. 2018;6(24):6398-6405.
16. Wright AD, Verdi C, Milot RL, et al. Electron-phonon coupling in hybrid lead halide perovskites. *Nat Commun*. 2016;7(1):11755.
17. Wang Y, Dar MI, Ono LK, et al. Thermodynamically stabilized β-$CsPbI_3$-based perovskite solar cells with efficiencies >18%. *Science*. 2019;365(6453):591-595.
18. Chang X, Fang J, Fan Y, et al. Printable $CsPbI_3$ perovskite solar cells with PCE of 19% via an additive strategy. *Adv Mater*. 2020;32(40):2001243.
19. Tao SX, Cao X, Bobbert PA. Accurate and efficient band gap predictions of metal halide perovskites using the DFT-1/2 method: GW accuracy with DFT expense. *Sci Rep*. 2017;7(1):14386.
20. Yang RX, Skelton JM, Silva EL, Frost JM, Walsh A. Spontaneous octahedral tilting in the cubic inorganic cesium halide perovskites $CsSnX_3$ and $CsPbX_3$ (X = F, CI, Br, I). *J Phys Chem Lett*. 2017;8(19):4720-4726.
21. Voloshinovskii AS, Myagkota SV, Pidzyrailo NS, Tokarivskii MV. Luminescence and structural transformations of $CsSnCl_3$ crystals. *J Appl Spectrosc*. 1994;60(3):226-228.
22. Brik MG. Comparative first-principles calculations of electronic, optical and elastic anisotropy properties of $CsXBr_3$ (X = Ca, Ge, Sn) crystals. *Solid State Commun*. 2011;151(23):1733-1738.
23. Becker MA, Vaxenburg R, Nedelcu G, et al. Bright triplet excitons in caesium lead halide perovskites. *Nature*. 2018;553(7687):189-193.
24. Hayatullah MG, Muhammad S, Naeem S, Khalid MN, Manzar A. Physical properties of $CsSnM_3$ (M = cl, Br, I): a first principle study. *Acta Phys Pol A*. 2013;124(1):102-107.
25. Yuan Y, Xu R, Xu H, Hong F, Xu F, Wang L. Nature of the band gap of halide perovskites ABX_3 (a = CH_3NH_3, Cs; B = Sn, Pb; X = cl, Br, I): first-principles calculations. *Chin Phys B*. 2015;24:116302.
26. Crespo CT. The effect of the halide anion on the optical properties of lead halide perovskites. *Sol Energy Mater Sol Cells*. 2019;195:269-273.
27. Yang RX, Skelton JM, Silva EL, Frost JM, Walsh A. Assessment of dynamic structural instabilities across 24 cubic inorganic halide perovskites. *J Chem Phys*. 2020;152(2):024703.
28. Handa T, Yamada T, Nagai M, Kanemitsu Y. Phonon, thermal, and thermo-optical properties of halide perovskites. *Phys Chem Chem Phys*. 2020;22(45):26069-26087.
29. Kashikar R, Khamari B, Nanda BRK. Second-neighbor electron hopping and pressure induced topological quantum phase transition in insulating cubic perovskites. *Phys Rev Mater*. 2018;2(12):124204.
30. Yu PY, Cardona M. *Fundamentals of Semiconductors: Physics and Materials Properties*. Berlin, Heidelberg; Springer; 2010.
31. Yang J, Wen X, Xia H, et al. Acoustic-optical phonon up-conversion and hot-phonon bottleneck in lead-halide perovskites. *Nat Commun*. 2017;8:14120.
32. Sui X, Gao X, Wu X, et al. Zone-folded longitudinal acoustic phonons driving self-trapped state emission in colloidal CdSe nanoplatelet superlattices. *Nano Lett*. 2021;21(10):4137-4144.
33. Li S, Luo J, Liu J, Tang J. Self-trapped excitons in all-inorganic halide perovskites: fundamentals, status, and potential applications. *J Phys Chem Lett*. 2019;10(8):1999-2007.
34. Wu B, Ning W, Xu Q, et al. Strong self-trapping by deformation potential limits photovoltaic performance in bismuth double perovskite. *Sci Adv*. 2021;7(8):eabd3160.
35. Zhang X, Xiao S, Li R, He T, Xing G, Chen R. Influence of mixed organic cations on the nonlinear optical properties of lead tri-iodide perovskites. *Photonics Res*. 2020;8(9):A25-A30.
36. Gautier R, Paris M, Massuyeau F. Exciton self-trapping in hybrid lead halides: role of halogen. *J Am Chem Soc*. 2019;141(32):12619-12623.
37. Mosconi E, Amat A, Nazeeruddin MK, Grätzel M, De Angelis F. First-principles modeling of mixed halide organometal perovskites for photovoltaic applications. *J Phys Chem C*. 2013;117(27):13902-13913.
38. Deschler F, Price M, Pathak S, et al. High photoluminescence efficiency and optically pumped lasing in solution-processed mixed halide perovskite semiconductors. *J Phys Chem Lett*. 2014;5(8):1421-1426.
39. Yu J, Kong J, Hao W, et al. Broadband extrinsic self-trapped exciton emission in Sn-doped 2D lead-halide perovskites. *Adv Mater*. 2019;31(7):1806385.
40. Li C, Wang A, Deng X, et al. Insights into ultrafast carrier dynamics in perovskite thin films and solar cells. *ACS Photonics*. 2020;7(8):1893-1907.
41. Ferdani DW, Pering SR, Ghosh D, et al. Partial cation substitution reduces iodide ion transport in lead iodide perovskite solar cells. *Energ Environ Sci*. 2019;12(7):2264-2272.
42. Aziz A, Aristidou N, Bu X, et al. Understanding the enhanced stability of bromide substitution in lead iodide perovskites. *Chem Mater*. 2020;32(1):400-409.
43. Rajeswarapalanichamy R, Amudhavalli A, Padmavathy R, Iyakutti K. Band gap engineering in halide cubic perovskites $CsPbBr_{3-y}I_y$ (y = 0, 1, 2, 3) - a DFT study. *Mater Sci Eng: B*. 2020;258:114560.
44. Ghaithan HM, Alahmed ZA, Qaid SMH, Hezam M, Aldwayyan AS. Density functional study of cubic, tetragonal, and orthorhombic $CsPbBr_3$ perovskite. *ACS Omega*. 2020;5(13):7468-7480.
45. Afsari M, Boochani A, Hantezadeh M, Elahi SM. Topological nature in cubic phase of perovskite $CsPbI_3$: by DFT. *Solid State Commun*. 2017;259:10-15.
46. Bose SK, Satpathy S, Jepsen O. Semiconducting $CsSnBr_3$. *Phys Rev B*. 1993;47(8):4276-4280.
47. Zheng J, Huan CHA, Wee ATS, Kuok MH. Electronic properties of $CsSnBr_3$: studies by experiment and theory. *Surf Interface Anal*. 1999;28(1):81-83.
48. Chabot JF, Cote M, Briere JF. *Ab Initio Study of the Electronic and Structural Properties of $CsSnI_3$ Perovskite*. National Research Council of Canada; 2003:57.
49. Harrison JF. On the role of the electron density difference in the interpretation of molecular properties. *J Chem Phys*. 2003;119(16):8763-8764.
50. Sanchez-Portal D, Artacho E, Soler JM. Projection of plane-wave calculations into atomic orbitals. *Solid State Commun*. 1995;95(10):685-690.
51. Mulliken RS. Electronic population analysis on LCAO-MO molecular wave functions. I. *J. Chem. Phys.* 1955;23(10):1833-1840.

52. Amudhavalli A, Rajeswarapalanichamy R, Padmavathy R, Iyakutti K. Electronic structure and optical properties of $CsPbF_{3-y}I_y$ (y = 0, 1, 2) cubic perovskites. *Acta Phys Pol A*. 2021;139(6):692-697.
53. Kronig RL. On the theory of dispersion of X-rays. *J Opt Soc Am*. 1926;12(6):547-557.
54. Jackson JD. *Classical Electrodynamics*. New York: Wiley; 1999.
55. Alù A, Silveirinha MG, Salandrino A, Engheta N. Epsilon-near-zero metamaterials and electromagnetic sources: tailoring the radiation phase pattern. *Phys Rev B*. 2007;75(15):155410.
56. Edwards B, Alù A, Young M, Silveirinha M, Engheta N. Experimental verification of epsilon-near-zero metamaterial coupling and energy squeezing using a microwave waveguide. *Phys Rev Lett*. 2008;100:033903.
57. Sun Q, Xu Y, Zhang H, et al. Optical and electronic anisotropies in perovskitoid crystals of $Cs_3Bi_2I_9$ studies of nuclear radiation detection. *J Mater Chem A*. 2018;6(46):23388-23395.
58. Zygmanski P, Sajo E. A self-powered thin-film radiation detector using intrinsic high-energy current. *Med Phys*. 2016;43(1):4-15.
59. Tanner DB. *Optical Effects in Solids*. Cambridge: Cambridge University Press; 2019.
60. Pérez-Osorio MA, Milot RL, Filip MR, et al. Vibrational properties of the organic-inorganic halide perovskite $CH_3NH_3PbI_3$ from theory and experiment: factor group analysis, first-principles calculations, and low-temperature infrared spectra. *J Phys Chem C*. 2015;119(46):25703-25718.
61. Guo P, Xia Y, Gong J, et al. Polar fluctuations in metal halide perovskites uncovered by acoustic phonon anomalies. *ACS Energy Lett*. 2017;2(10):2463-2469.
62. Marronnier A, Lee H, Geffroy B, Even J, Bonnassieux Y, Roma G. Structural instabilities related to highly anharmonic phonons in halide perovskites. *J Phys Chem Lett*. 2017;8(12):2659-2665.
63. Amudhavalli A, Padmavathy R, Rajeswarapalanichamy R, Iyakutti K. First-principles study of structural and optoelectronic properties of $CsSnI_{3-y}F_y$ (y = 0, 1, 2, 3) perovskites. *Indian J Phys*. 2020;94(9):1351-1359.
64. Kohn W. Image of the fermi surface in the vibration spectrum of metal. *Phys Rev Lett*. 1959;2(9):393-394.
65. Sun M, Huang B. Phonon evidence of Kohn anomalies in nanogenerator ZnO. *Nano Energy*. 2019;59:626-635.
66. Martin RM. *Electronic Structure: Basic Theory and Practical Methods*. Cambridge England: Cambridge University Press; 2004.
67. Satta J, Melis C, Carbonaro CM, et al. Raman spectra and vibrational analysis of $CsPbI_3$: a fast and reliable technique to identify lead halide perovskite polymorphs. *J Materiomics*. 2021;7(1):127-135.
68. Rousseau DL, Bauman RP, Porto SPS. Normal mode determination in crystals. *J Raman Spectrosc*. 1981;10(1):253-290.
69. Hamermesh M. *Group Theory and its Application to Physical Problems*. New York: Dover Publications; 1989.
70. Wei W, Li W, Butler KT, et al. An unusual phase transition driven by vibrational entropy changes in a hybrid organic-inorganic perovskite. *Angew Chem Int Ed*. 2018;57(29):8932-8936.

SUPPORTING INFORMATION

Additional supporting information may be found in the online version of the article at the publisher's website.

How to cite this article: Chen B, Sun M, Chen R, Huang B. Atomic substitution effects of inorganic perovskites for optoelectronic properties modulations. *EcoMat*. 2022;4(4):e12201. doi:10.1002/eom2.12201